Multigrid spatially constrained dispersion curve inversion: towards distributed acoustic sensing surface wave imaging

Jianbo Guan[1], Feng Cheng[1,2*],Jianghai Xia[1], Binbin Mi[1], Haoyuan Sun[1], and Jonathan B. Ajo-Franklin[2,3]

[1]School of Earth Sciences, Zhejiang University, 866 Yuhangtang Rd., Hangzhou, Zhejiang 310027, China

[2]Dept. of Earth, Environmental, and Planetary Sciences, Rice University, 6100 Main St., Houston, TX 77005, USA

[3]Lawrence Berkeley National Laboratory, 1 Cyclotron Rd., Berkeley, CA 94720, USA

Contents of Supporting Information

1. Figure S1: Comparison of Jacobian vectors in different parameter spaces. (a) 1D V_s model with low-and high-velocity layers. (b) The Jacobian vector at 24 Hz versus depth with (the blue dashed line) and without (the red dashed line) the logarithmic parameterization.

2. Figure S2: Schematic of a multidirectional differential operator based on a 2D discrete grid model. Each column represents a 1D layered model. The blue arrows represent the horizontal and vertical differential directions, and the red arrows represent the two diagonal directions.

3. Figure S3: 1DI inversion results for Grid s2 (the left panels), Grid s3 (the middle panels) and Grid s4 (the right panels). Included in each panel, in order from top to

bottom, the relative err of all dispersion data (a1, b1, c1), the root-mean-square-relative-error ($rmsre$) of dispersion data for each station (a2, b2, c2), the inverted 2D V_s model (a3, b3, c3), the model relative error at each discrete grid point (a4, b4, c4). The black dotted lines in (a3), (b3), and (c3) are the layer interfaces.

4. Figure S4: LCI inversion results for Grid s2 (the left panels), Grid s3 (the middle panels) and Grid s4 (the right panels). Included in each panel, in order from top to bottom, the relative err of all dispersion data (a1, b1, c1), the root-mean-square-relative-error ($rmsre$) of dispersion data for each station (a2, b2, c2), the inverted 2D V_s model (a3, b3, c3), the model relative error at each discrete grid point (a4, b4, c4). The black dotted lines in (a3), (b3), and (c3) are the layer interfaces.

5. Figure S5: The established initial V_s model in field application.

6. Figure S6: Data residuals from inversion results of different methods in field application. The root-mean-square relative-error between the observed dispersion curves and the predicted values of 1DI (a), LCI (b) and MCI (c). The solid ellipses and dashed ellipses encircle some area that have potentially contributed to the inversion uncertainty with large data residuals.

7. Figure S7: Comparisons between inverted 1D profiles of different methods (1DI, LCI and MCI) at locations 0.3 km (a), 15.5 km (b), and 27.6 km (c) with nearby borehole profiles.

8. Figure S8: Segment view (partitions: 19 km - 24 km) of the 2D V_s structure revealed by LCI with Grid f2 (a), Grid f3 (b), Grid f4 (c), and MCI (d), respectively. Two gray lines in each subfigure represent the depth variation along the DAS cable for velocity contour lines of 200 m/s and 270 m/s.

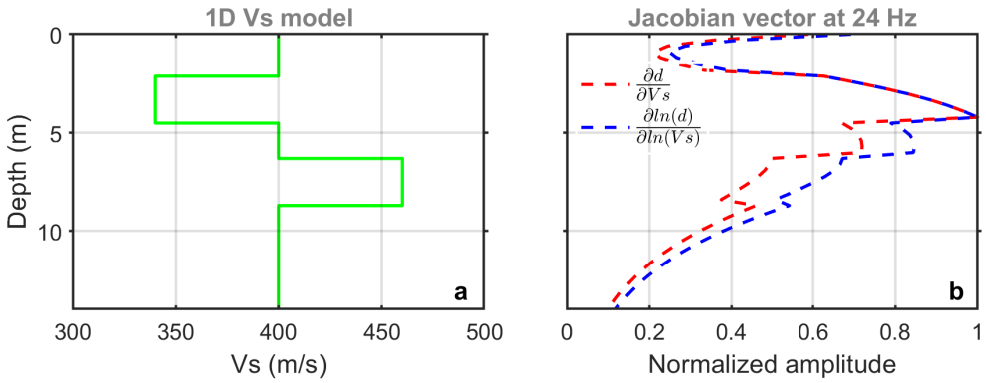

Figure S1. Comparison of Jacobian vectors in different parameter spaces. (a) 1D V_s model with low-and high-velocity layers. (b) The Jacobian vector at 24 Hz versus depth with (the blue dashed line) and without (the red dashed line) the logarithmic parameterization.

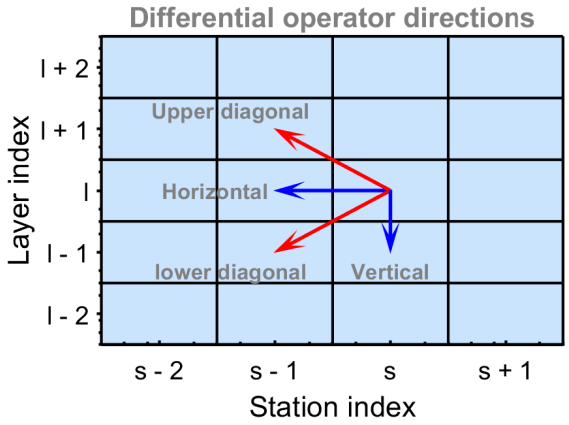

Figure S2. Schematic of a multidirectional differential operator based on a 2D discrete grid model. Each column represents a 1D layered model. The blue arrows represent the horizontal and vertical differential directions, and the red arrows represent the two diagonal directions.

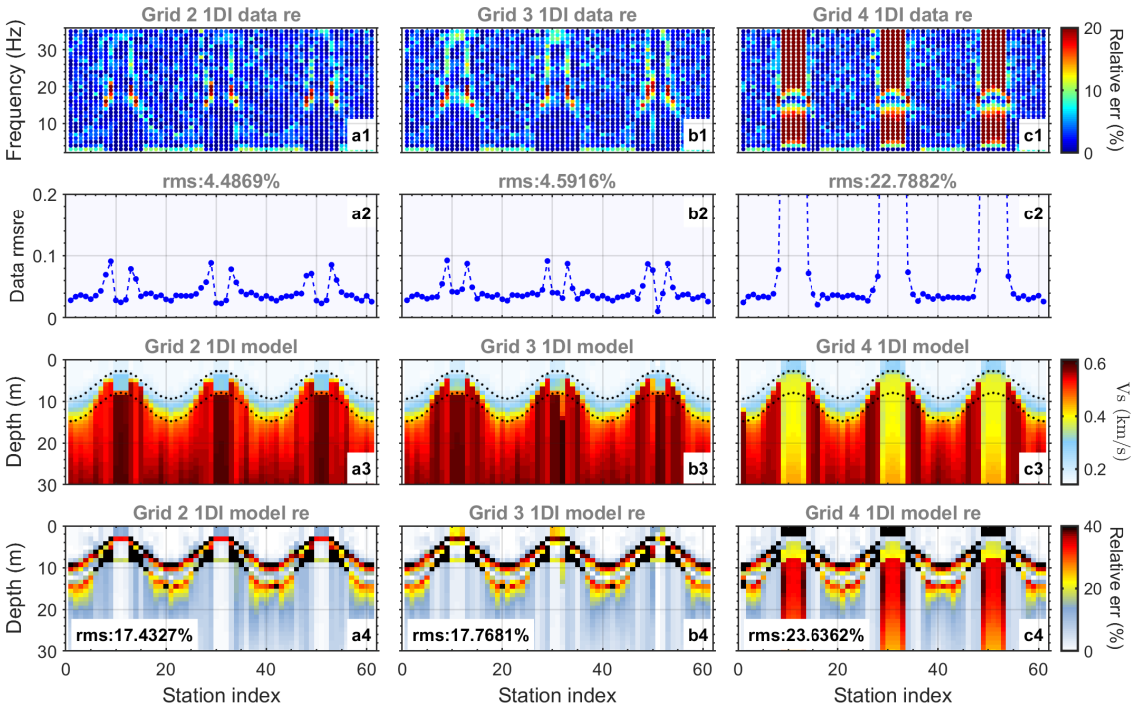

Figure S3. 1DI inversion results for Grid s2 (the left panels), Grid s3 (the middle panels) and Grid s4 (the right panels). Included in each panel, in order from top to bottom, the relative error of all dispersion data (a1, b1, c1), the root-mean-square-relative-error ($rmsre$) of dispersion data for each station (a2, b2, c2), the inverted 2D V_s model (a3, b3, c3), the model relative error at each discrete grid point (a4, b4, c4). The black dotted lines in (a3), (b3), and (c3) are the layer interfaces.

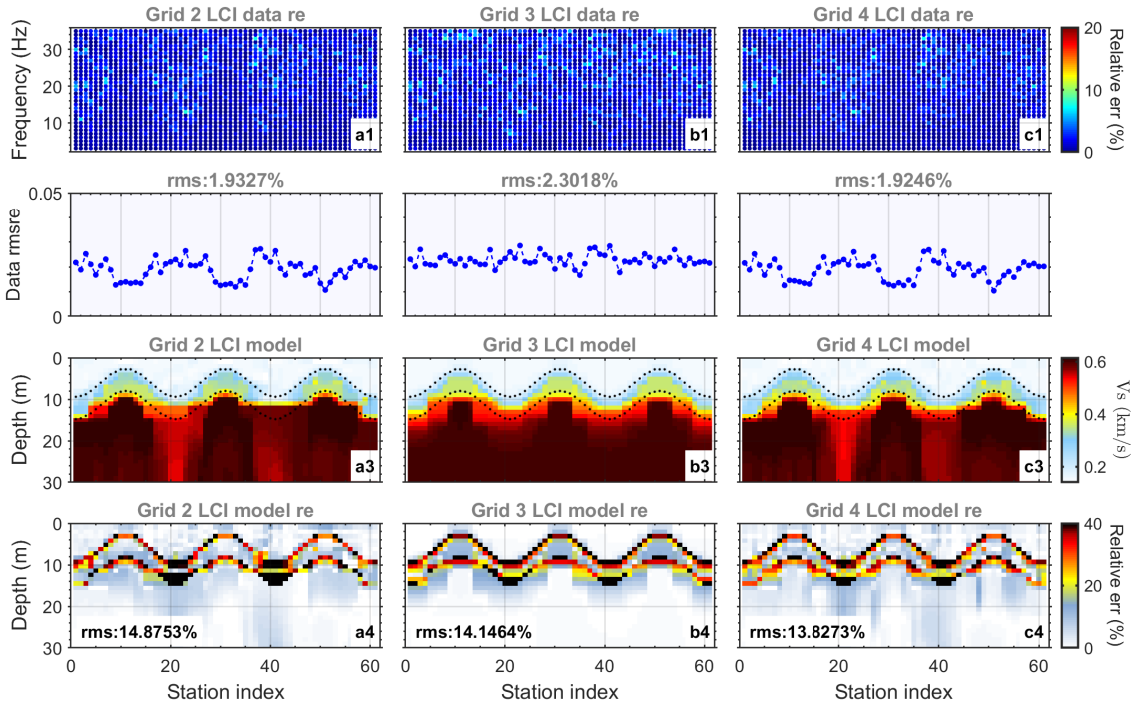

Figure S4. LCI inversion results for Grid s2 (the left panels), Grid s3 (the middle panels) and Grid s4 (the right panels). Included in each panel, in order from top to bottom, the relative err of all dispersion data (a1, b1, c1), the root-mean-square-relative-error ($rmsre$) of dispersion data for each station (a2, b2, c2), the inverted 2D V_s model (a3, b3, c3), the model relative error at each discrete grid point (a4, b4, c4). The black dotted lines in (a3), (b3), and (c3) are the layer interfaces.

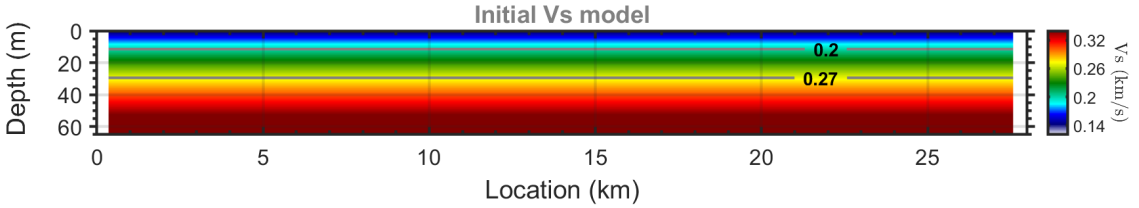

Figure S5. The established initial V_s model in field application.

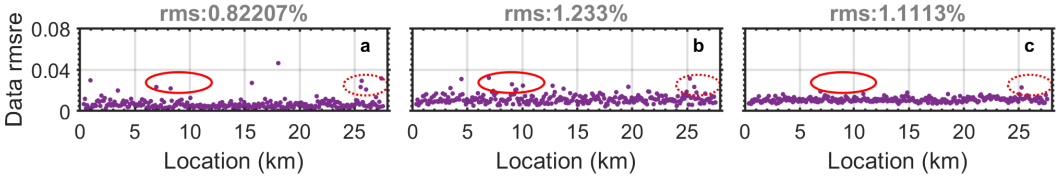

Figure S6. Data residuals from inversion results of different methods in field application. The root-mean-square relative-error between the observed dispersion curves and the predicted values of 1DI (a), LCI (b) and MCI (c). The solid ellipses and dashed ellipses encircle some area that have potentially contributed to the inversion uncertainty with large data residuals.

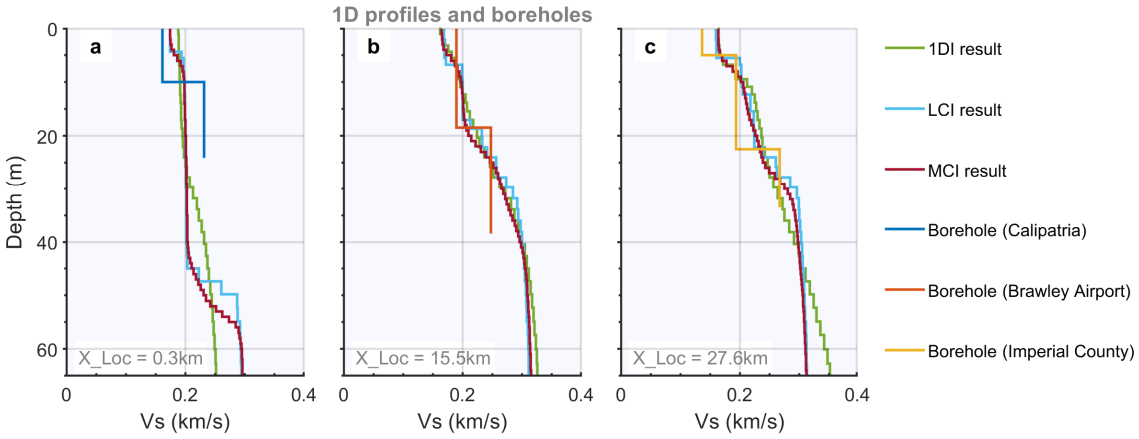

Figure S7. Comparisons between inverted 1D profiles of different methods (1DI, LCI and MCI) at locations 0.3 km (a), 15.5 km (b), and 27.6 km (c) with nearby borehole profiles.

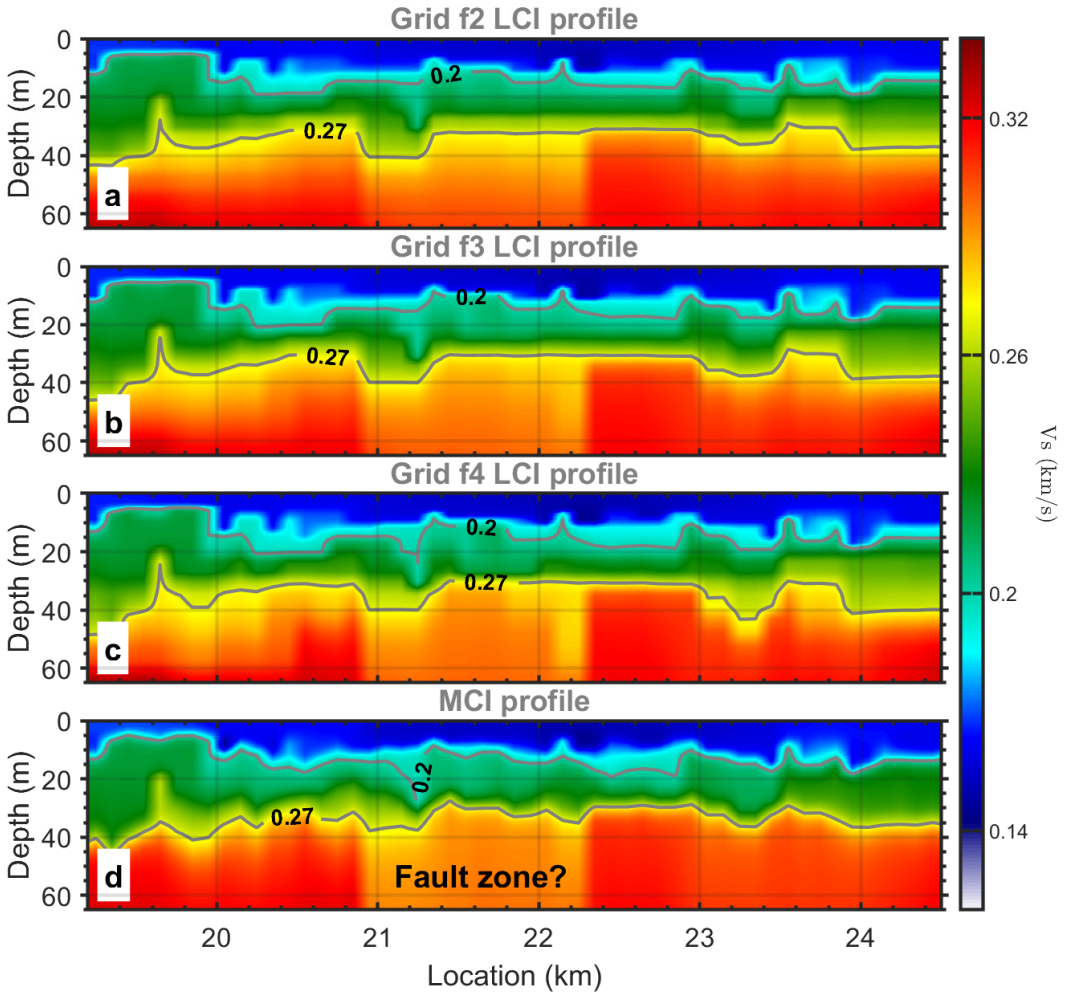

Figure S8. Segment view (partitions: 19 km - 24 km) of the 2D V_s structure revealed by LCI with Grid f2 (a), Grid f3 (b), Grid f4 (c), and MCI (d), respectively. Two gray lines in each subfigure represent the depth variation along the DAS cable for velocity contour lines of 200 m/s and 270 m/s.